Nano-scale modeling of rock-fluid interactions in low salinity water imbibition

Hamid Hosseinzade Khanamiri[1], Rasoul Khaledialidusti[1], Ole Torsaeter[1], Jan Aage Stensen[2]
[1]Norwegian University of Science and Technology
[2]Sintef Petroleum Research

This paper was prepared for presentation at the International Symposium of the Society of Core Analysts held in Avignon, France, 8-11 September, 2014

ABSTRACT

Causes of incremental oil recovery in low salinity waterflooding cannot precisely be described by bulk properties. Therefore studies in this area have been directed towards molecular scale phenomena and the proposed mechanisms so far can be classified at this scale. Since nano scale observations are challenging, there is not much research at this scale to verify the mechanisms. Molecular dynamics simulation is utilized in this study in order to understand the nano-scale aspect of low salinity process. Basal kaolinite and acetic acid represent the rock surface and polar hydrocarbon respectively. In-situ brine includes sodium and calcium chloride. Salinity gradient above the kaolinite surface was modeled according to double layer theory for a few nano-meters above the clay surface in two models. Rock, polar component and in-situ brine were the same in both models but the imbibing brines were a high salinity NaCl brine in high salinity model and pure water in low salinity model. All possible atomistic forces especially electrostatic and Van der Waals forces were considered to grasp the physics of the phenomenon.

Results show that acidic components are initially bonded strongly to the kaolinite surface by hydrogen bonds not by divalent cation bridges. Density profiles above clay surface show that desorption of acetic acid in low salinity model is more than in high salinity model. Also movement of calcium cations away from kaolinite surface in low salinity is more than in high salinity. Coordination of ions approves expansion of electrical double layer on clay surface in low salinity model. Results also show that electrical double layer of polar components expand too.

INTRODUCTION

Previously little attention has been given to composition of brine in water injection. Low salinity waterflooding can be an effective method of EOR where oil recovery is increased by only changing the brine chemistry. However identification of recovery mechanism(s) has been challenging. Counter examples were usually found to negate a proposed mechanism [1]. Zhang and Morrow [2] said that increase in oil recovery by low salinity flooding is highly specific to crude oil/brine/rock (COBR) combinations. Study of different cases may ultimately lead to recognition of low salinity injection mechanisms. The major proposed mechanisms are reviewed here.

Fines Migration: Tang and Morrow [3] believed that the migration of clay particles mainly kaolinite might be the cause for oil recovery upon injection of low salinity brine.

They hypothesized that heavy polar components of crude oil adsorb onto particles and pore walls resulting in mixed wetness; and changes in brine chemistry alters the forces required to desorb these particles from the pore walls during waterflooding. It was also believed that migration of fines leads to plugging of pore throats and permeability reduction resulting in flow diversion and sweep of unswept pores. Lemon et al [4] discussed that permeability decline may be useful for mobility control during waterflooding. Some laboratory works however showed increased oil recovery without fines production or significant permeability reduction [5].

Impact of desorbed fines on pore plugging and flow diversion cannot be directly concluded from increase in pressure drop. Pressure drop would increase upon desorption of oil or re-distribution of fluids while injection continues regardless of fines existence in the flowing fluids. Possibility of pore plugging by mineral particles can be judged by comparing size of the pore throats vs. size of the produced fine particles.

pH change: Austad et al [6] believed disturbance in brine-clay equilibrium is introduced and a local increase in pH at the clay surface is caused by desorption of active cations, especially Ca^{2+}, which is substituted by H^{+} from the water. A fast reaction between OH^{-} and the adsorbed acidic and protonated basic material would cause desorption of organic material from the clay. However Suijkerbuijk et al [7] observed that pH did not consistently rise in spontaneous imbibition experiments. In some experiments they observed even a substantial decrease in pH while significant oil was produced. They discussed that this hypothesis also implies that polar oil components and divalent cations compete to bind to rock surfaces instead of aiding each other in binding. This was not in line with their observations in which increasing divalent content of formation brine resulted in more oil wetness.

Multicomponent Ionic Exchange: Lager et al [5] introduced Multicomponent Ionic Exchange (MIE). It involves the competition between all the ions in the formation brine for the mineral exchange sites. Injection of low salinity brine is believed to result in MIE where polar components and organo-metallic complexes are replaced by uncomplexed cations. However Suijkerbuijk et al [8] discussed that as a consequence of ion exchange in the reservoir, a "*self-freshening zone*" is created separating the unchanged reservoir from the injected water composition by several pore volumes. Appelo [9] stated that in a low salinity environment divalent metal ions bind more strongly to the clays than in a high saline environment. This causes stripping of divalent cations from the injected low salinity brine leading to retardation of divalents [8]. Consequently increase in oil recovery at the salinity front cannot be due to MIE as the cation exchange takes place several pore volumes behind at the retardation front of divalents [8]. Consequently a mechanism other than MIE is the cause of oil recovery at the salinity front.

Double Layer Expansion: Ligthelm et al [10] believed that expansion of the electrical double layers is the cause of incremental oil recovery during low salinity injection. Based on experimental observations, they concluded that even though cation exchange may be partly responsible for the wettability change, it is the sufficient reduction in ionic strength and therefore increased repulsive electrostatic forces due to double layer expansion that plays the major role in wettability alteration.

Water Micro-Dispersions: Emadi and Sohrabi [11] studied low salinity injection by means of glass micro models. They observed formation of a dark colored material at oil/water interface during injection of low salinity brine, which they called *water micro-dispersions*. The micro-dispersions were not observed during injection of high salinity brine. Based on the observations, they presented two mechanisms: (1) wettability alteration is caused by alteration of the balance between binding and repulsive forces between oil/water and rock/water interfaces, (2) swelling of high salinity connate water droplets due to micro-dispersion coalescence at the oil/high salinity water interface.

Methodology

In this study, atom-level computer simulations are used to provide a comprehensive understanding of the properties of molecular assemblies. The simulations cover the time scale of a few nanoseconds and the length scale of a few nanometers. The molecular dynamics (MD) method is used to study complex systems to evaluate equilibrium and transport properties that cannot be calculated analytically. While these properties are determined at the atomic level, they are linked to the macroscopic properties of the bulk system through thermodynamics and statistical mechanics. All MD simulations were performed by using the Large Atomic/Molecular Massively Parallel Simulator (LAMMPS) package. MD produces time evolution of a system, the trajectory, by solving Newton's equation of motion (Equation 1) for the N-body system under the influence of specified forces. These equations are numerically integrated at given time intervals (~ 1femtoseconds). At every interval, a new set of particle positions and velocities is generated and used in the next set of integration.

$$m_i a(t)_i = F(x)_i = -\nabla E\big(x(t)\big)_i \qquad (1)$$

The total force acting on an atom is calculated from the first derivative of the atom's potential energy, as is shown on the right hand side of Equation (1). The forces and energies are evaluated using classical potential energy functions that describe interactions between atoms in the system called force fields.

In practice a basic MD simulation consists of the following steps: initialization, equilibration and dynamics run. The simulation is initiated by assigning atoms with initial positions and velocities. The next step is equilibrating the system in order to find the system in its minimum free energy. This is usually done by a preliminary run. This procedure leads to fluctuating the system's thermodynamic quantities, temperature and potential energy, around constant average values. When this is achieved the actual calculation run can be done.

The flexible potential is employed in this work to model inter and intramolecular interactions of all type of molecules in the clusters. The potential U is represented by

$$U\big(r_{ij}, \alpha_{ijk}\big) = u_{Bonded}\big(r_{ij}, \alpha_{ijk}\big) + u_{Non-Bonded}\big(r_{ij}\big), \qquad (2)$$

where the intramolecular potentials u_{Bonded} are given by,

$$u_{Bonded}\big(r_{ij}, \alpha_{ijk}\big) = u_{bond}\big(r_{ij}\big) + u_{angle}\big(\alpha_{ijk}\big) + \mathrm{U}_{\mathrm{dihedral}}\big(\theta_{\mathrm{ijkl}}\big), \qquad (3)$$

The intramolecular potentials $u_{\mathrm{bond}}\big(r_{\mathrm{ij}}\big)$, $u_{\mathrm{angle}}\big(\alpha_{\mathrm{ijk}}\big)$ and $u_{\mathrm{dihedral}}\big(\theta_{\mathrm{ijkl}}\big)$ represent the bond strength energy, bond angles energy and dihedral energy respectively. These three potential functions are given by

$$u_{bond}(r_{ij}) = \frac{1}{2}\sum_{bonds} K_r(r_{ij} - r_0)^2, \quad (4)$$

$$u_{angle}(\alpha_{ijk}) = \frac{1}{2}\sum_{\substack{bond\\angles}} K_\alpha(\alpha_{ijk} - \alpha_0)^2, \quad (5)$$

$$u_{dihedral}(\theta_{ijkl}) = \sum_{\substack{torsion\\(i,j,k,l)}} \sum_{n=1}^{N} k_{\theta_n}(1 + \cos(n\theta - \delta_n)) \quad (6)$$

where r_{ij}, α_{ijk}, r_0, α_0, K_r, K_α, k_θ and δ are the *ith* bond length, the ith bending angle, the equilibrium length of the bond in a molecule, the equilibrium angle of the bending angle, stiffness parameters for bond and angle, dihedral stiffness and equilibrium dihedral angle respectively. The intermolecular potentials $u_{Non-Bonded}$ are given by

$$u_{Non-Bonded}(r_{ij}) = u_{LJ}(r_{ij}) + u_{Coulomb}(r_{ij}), \quad (7)$$

$u_{LJ}(r_{ij})$ and $u_{Coulomb}(r_{ij})$ represent Lennard-Jones (Van der Waals) and Coulomb (electrostatic) potentials respectively. These two potential functions are given by

$$u_{LJ}(r_{ij}) = \sum_{atom\ pairs} \sum 4\epsilon[(\frac{\sigma}{r_{ij}})^{12} - (\frac{\sigma}{r_{ij}})^{6}], \quad (8)$$

$$u_{Coulomb}(r_{ij}) = \sum_{atom\ pairs} \sum \frac{q_i q_j}{4\pi\epsilon_0 r_{ij}}, \quad (9)$$

where ε, r_{ij}, σ, ϵ_0, q_i and q_j are the binding energy, the distance between a pair of i and j atoms, the molecular diameter, the electrical permittivity of space and the partial charges of the atoms within the cutoff distance. In the simulations, the cutoff distance is infinite (long-range) and thus Coulomb potential is calculated between all atoms in the system. Ewald summation method [12] was used for long-range electrostatic interactions. For the Lennard-Jones (Van der Waals) interactions a cutoff of 10.5Å was used. To compute the parameters for the mixed interaction, the Lorentz-Berthelot rule was employed [12].

$$\sigma_{ij} = \frac{1}{2}(\sigma_i + \sigma_j), \quad (10)$$

$$\epsilon_{ij} = \sqrt{\epsilon_i \epsilon_j}, \quad (11)$$

Simulation domain for the systems was considered as a cubic box with dimensions $L_xL_yL_z$ where L_x=12Å, L_y=17.6Å and L_z=120Å. In-situ brine which is the same in both models includes 20 Na^+ and 16 Ca^{2+} (number of cations). It also contains 12 molecules of CH_3COOH close to kaolinite surface. The model that represents high salinity has imbibing brine containing 8 Na^+ (number of ions). However the model that represents low salinity includes pure water as imbibing water. Since simulation of this model shows mixing of in-situ brine with fresh water, the term "low salinity" is used for this model. To reach equilibrium state, the NVE calculations were performed and for dynamic simulation the NVT was used. NVE is a system where number of molecules, volume and energy are constant and NVT is a system where number of molecules, volume and temperature are held constant. In these simulations, 0.25 nanosecond (ns) run in the NVE and 6.96 ns run in the NVT was performed and periodic boundary conditions were used. NVE included 500000 time steps of 0.2 femtosecond (fs) followed by 600000 time steps of 0.25 fs and NVT included 23200000 time steps of 0.3 fs in both models. Temperature was set to 60^0C and controlled by a Nose-Hoover thermostat [19, 20].

Table 1: values of non-bonded parameters

	Symbol	Mass (amu,1.6605×10^{-27}kg)	Charge (e)	ϵ (kcal/mol)	σ (Å)
Water oxygen	o	15.9994	-0.834	0.1521	3.1506
Water hydrogen	h	1.0080	+0.417	0.046	0.4
Hydroxyl oxygen in acetic acid	oh*	15.9994	-0.64484	0.1698	3.0
Double bound oxygen in acetic acid	oo*	15.9994	-0.59003	0.4122	2.6260
Hydroxyl hydrogen in acetic acid	hh*	1.008	+0.4333	0.0	0.0
Carbon in acetic acid	c*	12.011	+0.80105	0.097	3.361
Hydroxyl oxygen in clay	oh	15.9994	-0.95	0.1554	3.1655
Hydroxyl hydrogen in clay	hh	1.008	+0.425	0.0	0.0
Bridging oxygen in clay	ob	15.9994	-1.05	0.1554	3.1655
Tetrahedral silicon in clay	st	28.0855	+2.10	0.0000018405	3.3020
Octahedral aluminum in clay	ao	26.981539	+1.575	0.0000013298	4.2713
Methylene group	c3	15.035	+0.80105	0.1119	4.01
Chloride ion	Cl	35.4532	-1.00	0.1	4.40
Sodium ion	Na	22.9897	+1.00	0.0027	3.33
Calcium ion	Ca	40.078	+2.00	0.136363	2.80

Table 2: values of bond parameters

Bond stretch

species i	species j	K_r (Kcal/mol)	r_0(Å)
oh	hh	450.0	0.957
c3	c*	239.005	1.53
c*	oo*	600.0	1.230
c*	oh*	450.0	1.360
oh*	hh*	375.0	1.0
ao	ob	62.14	1.93
ao	oh	66.92	1.77
st	ob	99.185	1.63
st	oh	99.185	1.65

Angel bend

species i	species j	species k	K_α (Kcal/mol)	α_0 (deg)
h	o	h	55.0	104.52
c3	c*	oo*	60.0	121.0
c3	c*	oh*	60.0	115.0
oo*	c*	oh*	60.0	124.0
c*	oh*	hh*	47.5	109.5

Torsion

species i	species j	species k	species l	K_θ (Kcal/mol)	δ_n (deg)
c3	c*	oh*	hh*	4.0	180.0
oo*	c*	oh*	hh*	4.0	180.0

The flexible TIP3P-C water potential [13] is employed to model inter and intramolecular interactions of water molecules. All the bonded and non-bonded parameter

values for TIP3P-C model [13], clay structure [14], acetic acid molecule [15-17], calcium, sodium and chloride ions [18] are listed in Tables 1 and 2. Further information on molecular dynamics simulations is available in reference [12].

Results and discussion

Acetic acid and water: Figure 1 shows that desorption of acetic acid molecules from clay surface in low salinity model is more than that in high salinity. X-axis represents distance from the clay surface. Acetic acid molecules were initially in the interval of 5Å to 15Å from clay surface in both models. After 6.96ns – nano second – the farthest desorbed molecules in low salinity has a distance of around 50Å whereas less than 30Å in high salinity model. The maximum density of carboxylic acid at the end of simulation runs which occurs close to the surface of kaolinite is 0.9 and 0.7gr/cc respectively in high and low salinity while the initial value was 0.96gr/cc in both models. This shows that despite desorption of loosely bound polar molecules from the surface in high salinity, the majority of molecules are still close to the surface while in low salinity model desorption is more than high salinity.

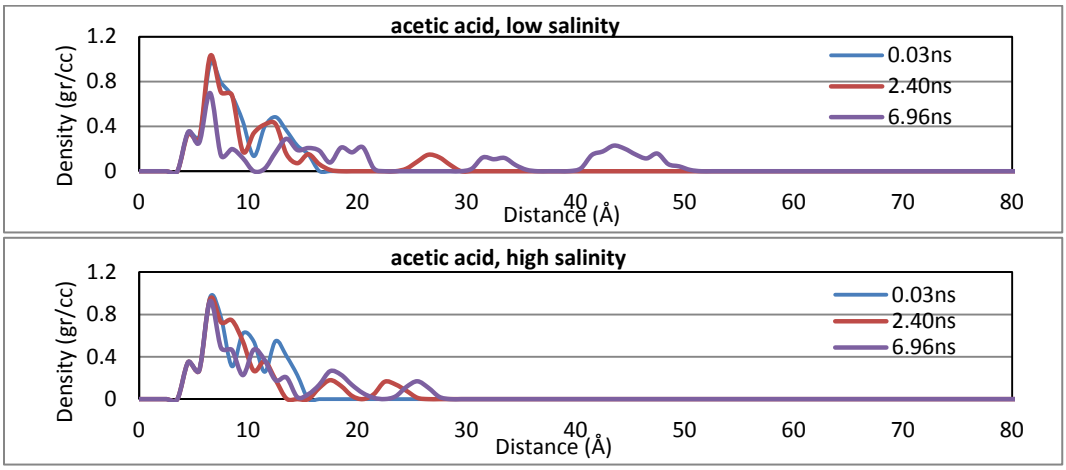

Figure 1: Density of acetic acid vs. distance from kaolinite surface at different time steps

Water density profile shows that in low salinity density increases close to rock surface more than in high salinity (Figure 2). This happens while acetic acid molecules are pushed away from the surface and displaced by water molecules. Figure 2 also shows that water molecules invaded into the clay crystal in low salinity model. The clay crystal is from 0 to 5Å. This invasion is even visible in the early time of simulation (0.03ns). There is no water invasion observed in high salinity model. The initial configuration, at *t* equals zero, of water molecules in both high and low salinity model was the same.

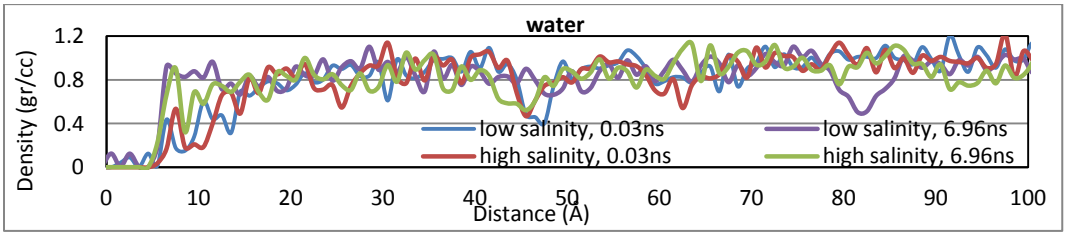

Figure 2: Density of water vs. distance from kaolinite surface at different time steps

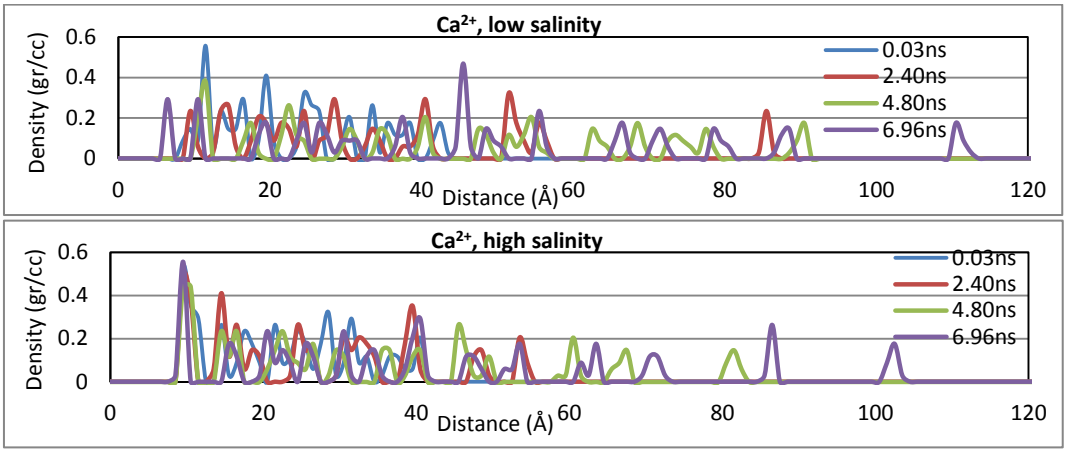

Figure 3: Density of Ca^{2+} vs. distance from kaolinite surface at different time steps

Ions: In low salinity water imbibition model, the density (concentration) of Ca^{2+} cations decreases vs. time (Figure 3). There is a substantial density reduction at 11.5Å from 0.56gr/cc at 0.03ns to 0.29gr/cc at 6.96ns. The opposite behavior observed in high salinity model. Density of Ca^{2+} cations has a marginal increase from 0.52gr/cc at 0.03ns to 0.55gr/cc at 6.96ns. In high salinity model, there is a marginal decrease in density close to surface at 9.5Å; however it eventually increases to 0.55gr/cc, a little higher than the initial density. The propagation of Ca^{2+} in the aqueous solution away from the surface in low salinity imbibition model is faster than the high salinity model. Advancing front of Ca^{2+} ions has reached to 85Å after 2.4ns; however it is at 53Å after 2.4ns in high salinity.

As noted, density of Ca^{2+} cations decreases dramatically close to surface in low salinity as shown in Figure 3. However there is a small shift of about 5Å of Ca^{2+} cations towards the surface. Simultaneously, in the interval of 10.5Å to 19.5Å, the density of Ca^{2+} reduces to zero in 6.96ns (Figure 4). In general, as the profiles show the Ca^{2+} cations moved away from the surface and the highest density was shifted from 11.5Å in 0.03ns to 45.5Å in 6.96ns. Furthermore, above 45.5Å, there is more Ca^{2+} cations in low salinity model than in high salinity model. The interval of 9.5Å to 15.5Å in high salinity model in 6.96ns is a calcium free zone too. However the difference between low and high salinity is that the maximum density in high salinity stays in 9.5Å from beginning till the end of simulation. Existence of these Ca^{2+} free zone close to rock surface in both models, especially in low salinity model where the desorption of Ca^{2+} is stronger than in high salinity, implies that Ca^{2+} cations encounter two forces which determine their coordination. These forces are attraction by clay surface and attraction by lower ionic strength imbibing water. In high salinity model, the outcome of these interactions is that the highest density close to the kaolinite surface remains the same as initial one which indicates strong attraction by clay to hold these divalent cations close to rock-fluid interface and the rest of divalents are distributed in the aqueous phase. This scattering in high salinity is weaker than in low salinity. Thus, in low salinity the attraction of Ca^{2+} cations by low ionic strength imbibing water is stronger. This is also an evidence of transfer of maximum Ca^{2+} density from 11.5Å to 45.5Å.

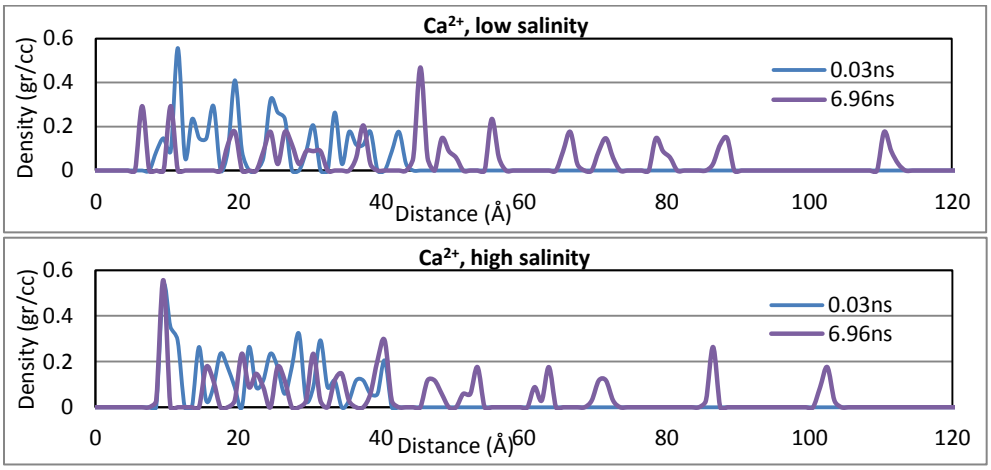

Figure 4: Density of Ca^{2+} vs. distance from kaolinite surface at initial and final time steps

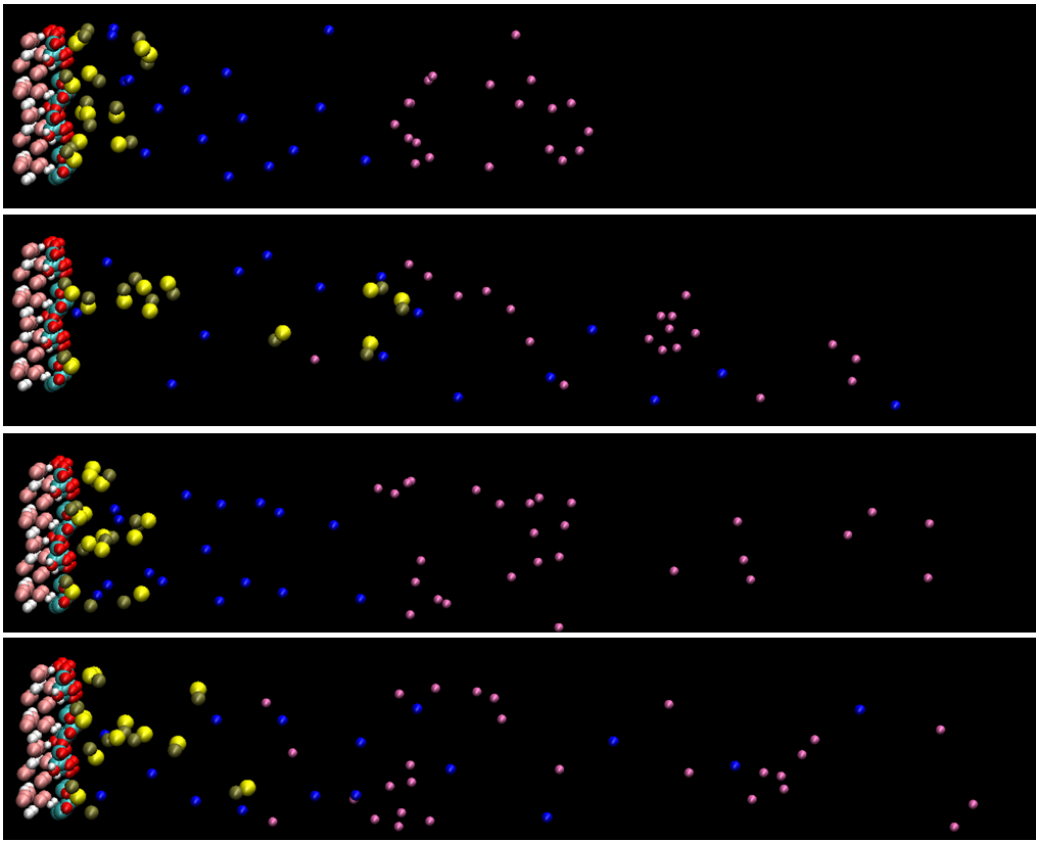

Figure 5: Top to bottom: Low salinity t=0, low salinity t=6.96ns, high salinity t=0; high salinity t=6.96ns. Colors: White (large): silicon, white (small): aluminum, dark pink: oxygen, red: hydrogen in hydroxyl group of kaolinite surface, turquoise: oxygen in hydroxyl group of kaolinite surface, yellow: O^- that has the double bond in CH_3COOH, brown: hydroxyl group of CH_3COOH, blue: Ca^{2+}, purple: Na^+; the rest of atoms are made invisible in the illustration. Z-axis is from left to right.

Furthermore, a comparison of density profiles of Ca^{2+}, acetic acid and water at different time steps demonstrates that desorption and movement of Ca^{2+} cations is faster than acetic acid molecules. This is true for both high salinity and low salinity models. Water

invasion rate into the clay structure in low salinity occurs as fast as to Ca^{2+} displacement. It seems that in low salinity quick movement of cations away from the kaolinite surface causes a counter current movement of water molecules towards the surface in a way that some water molecules can even penetrate into the clay crystal. This counter current movement can be partially responsible for desorption of polar components. Desorption of polar components occurs slower than desorption of Ca^{2+} and water penetration into the clay crystal. This implies that the attraction force (hydrogen bonds) between clay surface and these components is strong. These displacements and coordination of different species show that the factors play role in desorption of acetic acid molecules are expansion of double layer on the clay surface together with the counter current movement of water molecules towards the clay surface.

Figure 5 shows the coordination of different atoms in the initial and final conditions of simulations in both models. In these images initial time is t=0; however in the density profiles it is 0.03ns and the value of density at 0.03ns is an average of density in all the time steps from 0 to 0.03ns. This time interval is equivalent to 100,000 time steps.

Initially distance of Ca^{2+} cations and carboxylic acid molecules from the clay surface was nearly the same. During the equilibration of energy before start of the main imbibition run, Ca^{2+} cations changed their position to above carboxylic acid molecules. Therefore it seems that attraction between these molecules and the kaolinite surface is stronger than that of Ca^{2+} and the surface. As illustrated in Figure 6, acid molecules are bound to the surface by hydrogen bonds. This hydrogen bond has two forms: 1) the bond between the hydrogen of kaolinite hydroxyl group and oxygen with double bond in acid molecule and 2) the bond between the hydroxyl group of acid with oxygen in the kaolinite hydroxyl groups (Figure 6). In the first type the oxygen of acid (yellow) heads toward the hydrogen of kaolinite (red) hydroxyl group and in the second one the hydroxyl group in acid (brown) heads toward the oxygen in the kaolinite surface. In the second type of bond, since the oxygen of kaolinite is below its hydrogen and above the aluminum atoms, the acid molecules seem to be partially invaded into the crystal. At the start of the simulation in the low salinity imbibition model, there is also two Ca^{2+} cations in right side of the model in Figure 6 and one would say that these Ca^{2+} cations help the above one or two acid molecules in binding to the surface by divalent cation bridges. However, the majority of acid molecules are bound directly by hydrogen bonds to the surface. In the final time step, 6.96ns, when the acid molecules desorb from the surface, the remaining molecules on the surface still have hydrogen bonds. Adsorption of a couple of acid molecules to the surface can be attributed to the presence of a Ca^{2+} cation which is adsorbed to the surface.

Double layer of the polar component in aqueous phase: The distribution of ions in low and high salinity imbibitions were compared by means of radial distribution function (RDF). RDF shows how density varies vs. distance from a reference particle. Therefore RDF is equivalent to density or concentration of the ions around the reference particle. In Figure 7, oxygen which has the double bond with carbon atom in acetic acid (O^-) is the reference particle and density of different ions around it, is shown by RDF plots. RDFs were calculated up to a distance of 10.5Å from the reference particle with binning size of 0.5Å in the histograms.

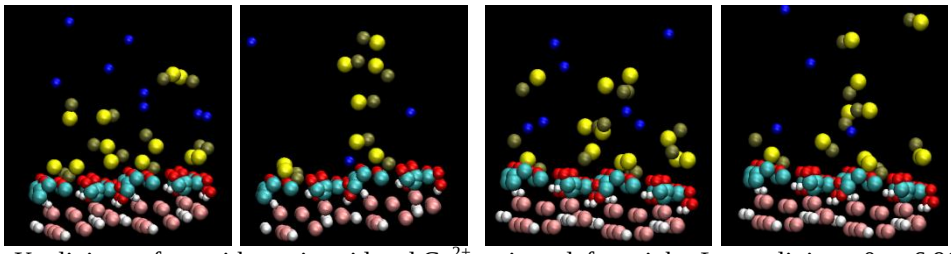

Figure 6: Kaolinite surface with acetic acid and Ca^{2+} cations, left to right: Low salinity t=0, t=6.96ns; high salinity t=0, t=6.96ns. Colors: the same as figure 5; the rest of molecules are made invisible.

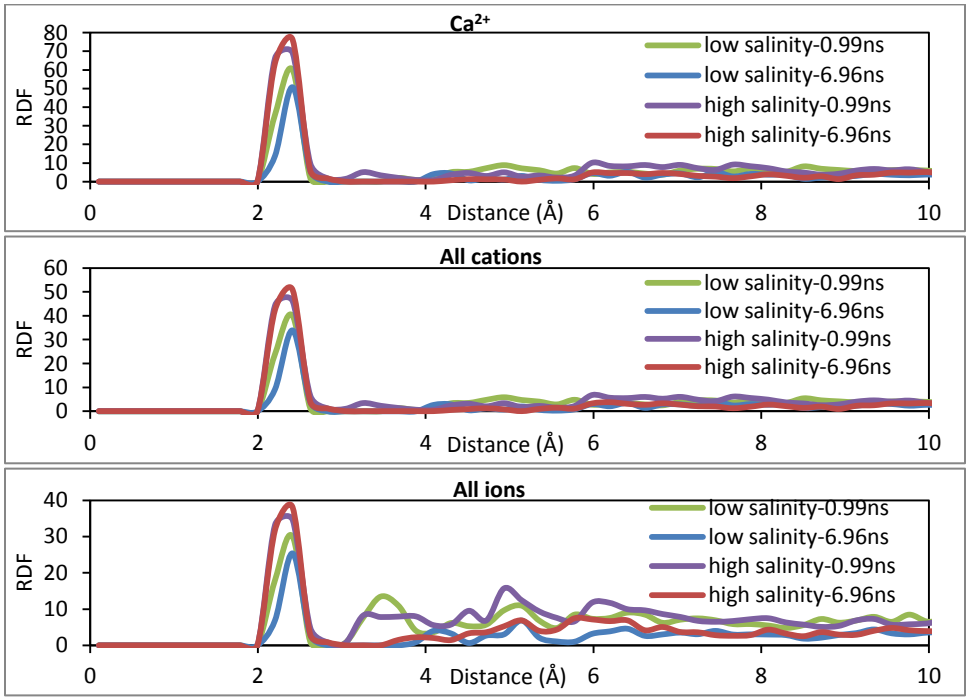

Figure 7: the reference particle in RDF calculations is the oxygen atom which has the double bond with carbon atom in acetic acid molecule; upper limits in y-axes are adjusted for better illustration

The plots in Figure 7 show that the density of calcium, all cations and all ions around the O^- of acetic acid molecules in high salinity is higher than that in low salinity. This implies that ions are more concentrated around the polar components in high salinity. In other words, the ions are less concentrated around the O^- in low salinity at the end of simulation. Additionally the maxima in all three plots are higher for high salinity and they occur at 2.41Å whereas for low salinity they occur at 2.62Å. The expansion based on the radius at which maximum density occurs is small; whereas based on the value of density (RDF), there is a major difference in high and low salinity imbibition models. The plots demonstrate that the concentrations of ions around acetic acid molecules are increased in high salinity whereas decreased in low salinity. This is the direct confirmation for expansion of electrical double layer of the polar component. Thus, in addition to expansion of electrical double layer on the kaolinite surface, expansion of double layer has occurred on the oil-water interface too.

After desorption of a polar oil component from the rock surface, oil must travel a long way before it reaches the production well. Accumulation of single molecules to form small droplets, formation of oil ganglia and bulk must occur successfully to have a continuous oil phase movement. In this process, desorbed oil can be re-adsorbed in rock surfaces. Expansion of electrical double layer around the oil molecules in low salinity may reduce the possibility of re-adsorption by providing thicker hydrated shield.

CONCLUSION

Nano scale simulation of low and high salinity led to the following conclusions:

- Ca^{2+} cations quickly move away from the kaolinite surface in low salinity model. Counter current movement of water molecules towards the kaolinite surface occurs quickly too. However desorption of acetic acid molecules is a slower process compared to the movement of Ca^{2+} and water.
- The point close to the kaolinite surface at which Ca^{2+} has maximum density shifts considerably away from the surface in low salinity model. This shows double layer expansion. In high salinity, however the maximum density remains close to surface.
- Double layer of acetic acid molecules expands in low salinity. This may avoid re-adsorption of those molecules.

ACKNOWLEDGEMENTS

Authors would like to appreciate financial support of Research Council of Norway, Unger Surfactants, Statoil, Lundin Norge AS, Det Norske and GDF Suez.

REFERENCES

1. Sheng J. J., "Modern Chemical Enhanced Oil Recovery, Theory and Practice," Gulf publishing, 2011, p. 51–78
2. Zhang, Y. and Morrow, N.R., "Comparison of secondary and tertiary recovery with change in injection brine composition for crude oil/sandstone combinations," Paper SPE 99757 presented at 2006 SPE/DOE Symposium on Improved Oil Recovery, Tulsa, OK, USA, 22-26 Apr 2006
3. Tang G.Q. and Morrow N.R., "Influence of brine composition and fines migration on crude oil/brine/rock interactions and Oil Recovery," J. of Pet. Sci. Eng. 24, 1999, 99-11
4. Lemon, P. Zeinijahromi A., Bedrikovetsky P., Shahin I., "Effects of Injected-Water Salinity on Waterflood Sweep Efficiency through Induced Fines Migration," Journal of Canadian Petroleum Technology 50.9-10, 2011, pp. 82-94
5. Lager, A., Webb, K.J., Black, C.J.J, Singleton, M., Sorbie, K.S., "Low Salinity Recovery – An Experimental Investigation," Paper SCA2006-36 presented at International Symposium of the SCA in Trondheim, Norway, 12-16 Sep 2006
6. Austad, T., RezaeiDoust, A., Puntervold, T., "Chemical Mechanism of Low Salinity Water Flooding in Sandstone Reservoirs, " Paper SPE 129767 presented at the SPE Improved Oil Recovery Symposium in Tulsa, Oklahoma, USA, 24-28 Apr 2010

7. Suijkerbuijk, B.M.J.M., Hofman, J.P., Ligthelm, D.J., Romanuka, J., Brussee, N., Van der Linde, H.A., Marcelis, A.H.M., "Fundamental investigations into wettability and low salinity flooding by parameter isolation," SPE 154204 presented at 18th SPE IOR Symposium in Tulsa, Oklahoma, USA, 14–18 Apr 2012
8. Suijkerbuijk, B.M.J.M, Kuipers H.P.C.E., Van Kruijsdijk C.P.J.W., Berg S., Van Winden J.F., Ligthelm D.J., Mahani H., Pingo Almada M., Van den Pol E., Joekar Niasar V., Romanuka J., Vermolen E.C.M., Al-Qarshubi I.S.M., "Development of a Workflow to Improve Predictive Capability of Low Salinity Response," Paper IPTC 17157 presented at International Petroleum Technology Conference in Beijing, China, 2013
9. Appelo, C.A.J., "Cation and proton exchange, pH, variations, and carbonate reactions in a freshening aquifer, " Water Resources Research 1994, 30, 2793–2805
10. Ligthelm, D.J., Gronsveld, J., Hofman, J.P., Brussee, N.J., Marcelis, F., Van der Linde, H.A., "Novel Waterflooding Strategy by Manipulation of Injection Brine Composition," Paper SPE 119835 presented at SPE EUROPEC/EAGE Annual Conference and Exhibition in Amsterdam, Netherlands, 8–11 Jun 2009
11. Emadi, A., Sohrabi M., "Visual Investigation of Oil Recovery by Low Salinity Water Injection: Formation of Water Micro-Dispersions and Wettability Alteration," Paper SPE 166435 presented at SPE Annual Technology Conference and Exhibition in New Orleans, Louisiana, USA, 30 Sep- 2 Oct 2013
12. Rapaport, D.C., The Art of Molecular Dynamics Simulation, 2nd Edition, Cambridge University Press, 2004
13. Griebel, M., Knapek, S., Zumbusch, G., "Numerical Simulation in Molecular Dynamics," Springer, Berlin, 2007
14. Stellpflug, A., Nicholas, J. B., Carrado, K. A., Keldsen, G., Winans, R. E., "Development of a Molecular Mechanics Force Field for Clays: I. Structure And IR Spectra of Kaolinite," presented in Symposium on Computer Applications in Fuel Chemistry, 1991 Spring (Atlanta) 36(1)
15. Gavezzotti, A., "A molecular dynamics view of some kinetic and structural aspects of melting in the acetic acid crystal," Journal of Molecular Structure 485-486 August 1999, p. 485-499
16. Capaldi, F.M., Boyce, M.C., "Molecular response of a glassy polymer to active deformation," Polymer, 45(4), Feb 2004, p. 1391-1399
17. Ma, X., Chakraborty, P., Henz B. J., Zachariah, M. R., "Molecular dynamic simulation of dicarboxylic acid coated aqueous aerosol: structure and processing of water vapor" Phys. Chem. Chem. Phys., 2011, 13, 9374-9384
18. Mamatkulov, S., Fyta M., Netz, R. R., "Force fields for divalent cations based on single-ion and ion-pair properties" the Journal of Chem. Phys., 2013, 138, 024505
19. Nosé, S., "A unified formulation of the constant temperature molecular dynamics methods" J. Chem. Phys., 1984, 81, p. 511-519
20. Hoover, W. G., "Canonical dynamics: Equilibrium phase-space distributions" Phys Rev A, 1985, 31, p.1695–1697